International Journal for Multidisciplinary Research (IJFMR)
E-ISSN: 2582-2160 ● Website: www.ijfmr.com ● Email: editor@ijfmr.com

Hydrothermal Synthesis and Visible-Light Photocatalytic Activity of Bi_2WO_6, Bi_2MoO_6, and Mixed $Bi_2W_{1-x}Mo_xO_6$ Oxides for Efficient Methylene Blue Degradation

Bandi Ashok[1], Madhu Darmapuri[2], M. Satyanarayana[3]

[1]SRR Government Arts & Science College, Karimnagar, Telangana-505001
[2] Government Degree College, Hayathnagar, Rangareddy, Hyderabad, Telangana-501505
[3]Government Degree College, Rajendranagar, Shamshabad, Hyderabad, Telangana-501218

Abstract

Visible-light-driven photocatalysts based on Bi_2WO_6, Bi_2MoO_6, and their mixed compositions $Bi_2W_{0.75}Mo_{0.25}O_6$ and $Bi_2W_{0.25}Mo_{0.75}O_6$ were successfully synthesized by a hydrothermal method. X-ray diffraction confirmed the formation of phase-pure orthorhombic structures, while FESEM analysis revealed distinct morphologies such as rods, spheres, and plate-like nanostructures. X-ray photoelectron spectroscopy verified the presence of Bi^{3+}, W^{6+}, Mo^{6+}, and O^{2-}, and FTIR spectra supported the successful formation of the target compounds through characteristic vibrational features. The optical band gaps of the prepared samples were evaluated to assess their visible-light absorption behavior. The photocatalytic performance was examined through the degradation of Methyleneene Blue under visible light irradiation for up to 240 min. The blank experiment showed negligible degradation, whereas Bi_2WO_6 and Bi_2MoO_6 achieved degradation efficiencies of 68% and 65%, respectively. Remarkably, the mixed oxides $Bi_2W_{0.75}Mo_{0.25}O_6$ and $Bi_2W_{0.25}Mo_{0.75}O_6$ exhibited much higher efficiencies of 94% and 96%, respectively, indicating a strong synergistic effect in enhancing photocatalytic activity. Scavenger experiments revealed that superoxide radicals ($\bullet O_2^-$) and photogenerated holes (h^+) were the major reactive species involved in the degradation process. These results demonstrate that the mixed Bi-based oxides are highly promising visible-light photocatalysts for the efficient removal of dye pollutants.

Keywords: Hydrothermal synthesis, Bismuth-based oxides, Photocatalysis, Methylene Blue degradation

1. Introduction

Methyleneene Blue is a synthetic dye extensively used in textile dyeing, printing, finishing, and several industrial coloring applications. The discharge of untreated industrial wastewater containing dye pollutants into natural water bodies has become a serious environmental concern. Such contaminants not only affect aquatic ecosystems but also pose significant risks to human health. Since water is an essential resource for all living organisms, the treatment and decolorization of industrial wastewater have become crucial for environmental protection and public health. Consequently, the removal of dye pollutants from wastewater has attracted increasing research interest in recent years [1,2].

A major breakthrough in photocatalysis was achieved in 1972 when Fujishima and Honda demonstrated the photoelectrochemical splitting of water using a TiO_2 electrode under ultraviolet light irradiation [3]. Since then, TiO_2 has been widely investigated for the degradation of organic pollutants and dye molecules because of its strong oxidation ability, excellent chemical stability, non-toxicity, and low cost. However, the practical application of TiO_2 under visible light is limited due to its wide band gap (3.2 eV) and the rapid recombination of photogenerated electron–hole pairs [4]. As visible light constitutes the major portion of solar radiation, the development of efficient visible-light-responsive photocatalysts with narrower band gaps is highly desirable. In recent years, several bismuth-based semiconductors such as $BiVO_4$, Bi_2WO_6, Bi_2MoO_6, and Bi_2O_3 have emerged as promising visible-light-driven photocatalysts because of their suitable electronic structures and narrow band gaps. Furthermore, the incorporation of suitable dopants or mixed metal ions into these semiconductors has been reported to significantly enhance their photocatalytic performance. Examples include Sn-doped Bi_2MoO_6, Ce-doped Bi_2WO_6, and Ni-doped $BiVO_4$. Among these materials, Bi_2WO_6 and Bi_2MoO_6 have received considerable attention due to their excellent photocatalytic efficiency, chemical stability, and strong visible-light absorption properties [5–7].

In the present work, Bi_2WO_6, Bi_2MoO_6, $Bi_2W_{0.75}Mo_{0.25}O_6$, and $Bi_2W_{0.25}Mo_{0.75}O_6$ photocatalysts were selected to investigate and compare their photocatalytic activities. Bi_2WO_6 and Bi_2MoO_6 belong to the Aurivillius family of layered oxides and consist of alternating perovskite-like WO_6 or MoO_6 octahedral layers. In the mixed compositions, Mo ions partially substitute W sites while maintaining the layered orthorhombic structure. These materials exhibit excellent thermal and chemical stability, enhanced visible-light absorption, and reduced recombination of photogenerated charge carriers, which contribute significantly to their photocatalytic performance [11–13]. Therefore, the present study focuses on the synthesis of orthorhombic Bi_2WO_6, Bi_2MoO_6, $Bi_2W_{0.75}Mo_{0.25}O_6$, and $Bi_2W_{0.25}Mo_{0.75}O_6$ semiconductors and the evaluation of their photocatalytic activities under visible-light irradiation.

2. Experimental details

2.1. Synthesis of Bi_2WO_6, Bi_2MoO_6, $Bi_2W_{0.75}Mo_{0.25}O_6$ and $Bi_2W_{0.25}Mo_{0.75}O_6$

Bi_2WO_6 was synthesized using a hydrothermal method. Initially, 1.41 g of $Bi(NO_3)_3 \cdot 5H_2O$ was dissolved in 30 mL of double-distilled water under continuous magnetic stirring for 30 min. A few drops of dilute HNO_3 were added to obtain a clear and homogeneous solution, designated as solution A. Separately, 0.40 g of $Na_2WO_4 \cdot 2H_2O$ was dissolved in 20 mL of double-distilled water and stirred for 30 min to prepare solution B. Solution B was added slowly to solution A with continuous stirring for another 30 min, resulting in the formation of a uniform white precursor suspension with an initial pH of about 2. The pH of the mixture was then adjusted to 6 by adding dilute NaOH solution. The obtained suspension was transferred into a 100 mL Teflon-lined stainless-steel autoclave and maintained at 180 °C for 12 h under hydrothermal conditions. After natural cooling to room temperature, the precipitate was collected and washed several times with double-distilled water and ethanol to remove residual impurities. The final product was dried overnight at 60 °C in a hot-air oven and subsequently ground into fine powder.

Bi_2MoO_6 was synthesized under similar experimental conditions using 1.61 g of $Bi(NO_3)_3 \cdot 5H_2O$ and 0.38 g of $Na_2MoO_4 \cdot 2H_2O$ as precursor materials. For the preparation of mixed oxide samples $Bi_2W_{1-x}Mo_xO_6$ (x = 0.25 and 0.75), the same hydrothermal procedure was followed. In a typical synthesis, 1.55 g of $Bi(NO_3)_3 \cdot 5H_2O$ was dissolved in 30 mL of double-distilled water to form solution A. Separately, $Na_2WO_4 \cdot 2H_2O$ and $Na_2MoO_4 \cdot 2H_2O$ were dissolved in 20 mL of double-distilled water to

prepare solutions B and C, respectively. The precursor solutions were slowly mixed with solution A under constant stirring for 30 min to form a homogeneous white suspension. The resulting mixture was transferred into a Teflon-lined stainless-steel autoclave and heated at 180 °C for 12 h. After cooling naturally to room temperature, the precipitate was washed repeatedly with distilled water and ethanol, followed by drying at 60 °C overnight to obtain $Bi_2W_{0.75}Mo_{0.25}O_6$. The $Bi_2W_{0.25}Mo_{0.75}O_6$ sample was synthesized similarly by adjusting the molar ratio of tungsten and molybdenum precursors.

3. Photocatalytic activity(PCA)

The PCA of the synthesized compounds was investigated under visible-light irradiation using Methylene Blue (MB) as the model organic pollutant. In a typical experiment, 50 mg of the photocatalyst was dispersed in 50 mL of 10^{-5} M aqueous MB solution. Prior to light irradiation, the suspension was magnetically stirred in the dark for 1 h to establish adsorption–desorption equilibrium between the dye molecules and the catalyst surface. After achieving equilibrium, the reaction mixture was exposed to visible light generated from a 200 W tungsten filament lamp placed inside a photochemical reactor. During the photocatalytic process, 4 mL aliquots were collected from the reaction mixture at regular intervals of 30 min and centrifuged at 5000 rpm for 15 min to separate the photocatalyst particles. The concentration of the remaining MB dye was determined using a UV–Vis spectrophotometer by measuring the absorbance at the maximum absorption wavelength of 663 nm. The photocatalytic degradation efficiency of MB was calculated using the following equation

$$.Degradation(\%) = \frac{C_0 - C_t}{C_0} \times 100 (1)$$

where C_0 = initial concentration of MB and C_t = concentration of MB at 't'min.

4. Results and Analysis

4.1. XRD treatment

X-ray diffraction (XRD) studies were performed to examine the crystal structure, phase purity, and crystallinity of the synthesized photocatalysts. The XRD patterns of Bi_2WO_6, Bi_2MoO_6, $Bi_2W_{0.75}Mo_{0.25}O_6$, and $Bi_2W_{0.25}Mo_{0.75}O_6$ are displayed in Fig. 1. For Bi_2MoO_6, the diffraction peaks observed at 28.23°, 32.59°, 46.66°, 56.22°, and 58.39° correspond to the crystal planes (131), (200), (202), and (331)/(262)/(220), respectively. These diffraction peaks are in good agreement with the standard JCPDS data card No. 84-0787, confirming the formation of orthorhombic Bi_2MoO_6. The calculated lattice parameters were determined to be (a = 5.487) Å, (b = 5.506) Å, and (c = 16.226) Å [14,15]. In the case of Bi_2WO_6, $Bi_2W_{0.75}Mo_{0.25}O_6$, and $Bi_2W_{0.25}Mo_{0.75}O_6$, the major diffraction peaks appeared at approximately 28.39°, 32.90°, 47.13°, 55.97°, 58.54°, 69.14°, 76.14°, and 78.65°. These peaks were indexed to the crystal planes (131), (200), (202), (133), (226), (400), (102), and (204), respectively. The observed diffraction peaks closely match the orthorhombic phase of Bi_2WO_6 according to JCPDS card No. 39-0256 [16]. The diffraction patterns of all the synthesized samples exhibited sharp and intense peaks, indicating good crystallinity and phase purity. Since all the samples possess similar orthorhombic crystal structures, their diffraction patterns appear nearly identical. No impurity peaks corresponding to secondary phases or separate molybdenum compounds were detected, suggesting the successful incorporation of Mo ions into the Bi_2WO_6 lattice. A slight shift in the diffraction peaks associated with the (131) and (200) planes was observed for the mixed oxide samples $Bi_2W_{0.75}Mo_{0.25}O_6$

and $Bi_2W_{0.25}Mo_{0.75}O_6$. The peak shift became more pronounced with increasing Mo content, which may be attributed to lattice distortion caused by the substitution of W^{6+} ions by Mo^{6+} ions within the crystal structure [17].

The average crystallite size ((D)) of the synthesized samples was estimated using the Debye–Scherrerequation from the full width at half maximum (FWHM) of the most intense diffraction peak corresponding to the (131) plane [18]

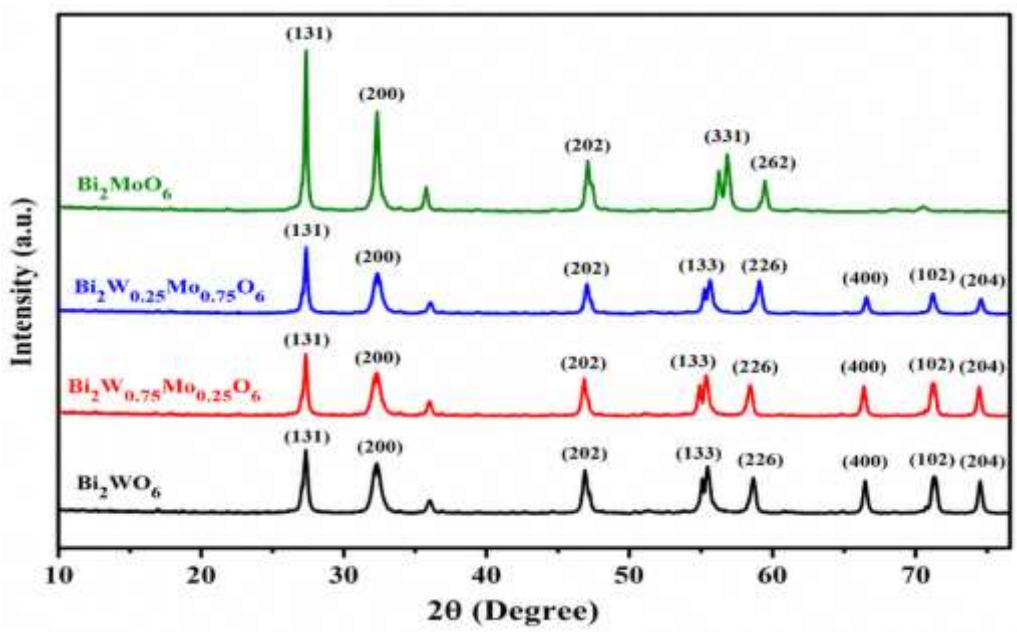

Figure 1. XRD patterns of Bi_2WO_6, Bi_2MoO_6, $Bi_2W_{0.75}Mo_{0.25}O_6$ and $Bi_2W_{0.25}Mo_{0.75}O_6$,

$$D = \frac{0.9\lambda}{\beta cos\theta} \qquad (2)$$

where D, λ, β, and θ correspond to the average crystallite size, X-ray wavelength, FWHM, and the Bragg diffraction angle (in radians) of the respective crystal plane, respectively. The calculated crystallite sizes of Bi_2WO_6, Bi_2MoO_6, $Bi_2W_{0.75}Mo_{0.25}O_6$, and $Bi_2W_{0.25}Mo_{0.75}O_6$ were approximately 20, 39, 24, and 20 nm, respectively. The variation in crystallite size may be related to the different Mo concentrations, which can introduce lattice strain and structural distortion into the crystal framework.

4.2. Field Emission Scanning Electron Microscopy (FESEM)

Figure 2(a–d) presents the FESEM images of Bi_2WO_6, Bi_2MoO_6, $Bi_2W_{0.75}Mo_{0.25}O_6$, and $i_2W_{0.25}Mo_{0.75}O_6$ photocatalysts. The FESEM image of Bi_2WO_6 reveals the presence of irregularly shaped nanostructures predominantly composed of rod-like and plate-like particles. In contrast, Bi_2MoO_6 exhibits agglomerated nanoplatelet-type morphologies. The particle size observed in Bi_2MoO_6 appears to be slightly larger than that of Bi_2WO_6. The mixed oxide samples $Bi_2W_{0.75}Mo_{0.25}O_6$ and $Bi_2W_{0.25}Mo_{0.75}O_6$ consist of aggregated non-uniform plate-like and spherical nanostructures. The particle size of these mixed compositions is comparatively smaller than that of pure Bi_2WO_6 and Bi_2MoO_6. Furthermore, a higher degree of agglomeration was observed in $Bi_2W_{0.25}Mo_{0.75}O_6$ compared to $Bi_2W_{0.75}Mo_{0.25}O_6$, as shown in Figure 2(c–d). These morphological observations are in good agreement with previously reported studies [19,20]. To further investigate the elemental composition of the synthesized samples, EDX spectra along with mixed and individual elemental mapping analyses were carried out, as presented in Figure 3(i–iv). The EDX results confirmed the presence of the constituent elements corresponding to each

compound, indicating the successful formation of the desired materials. The EDX spectrum of $Bi_2W_{0.25}Mo_{0.75}O_6$ confirmed the presence of Bi, Mo, and O elements, whereas the mixed oxide sample $Bi_2W_{0.75}Mo_{0.25}O_6$ showed the existence of Bi, W, Mo, and O elements in appropriate proportions. In addition, elemental mapping analysis demonstrated the uniform distribution of Mo atoms within the Bi_2WO_6 matrix, confirming the successful incorporation of Mo into the crystal structure of $Bi_2W_{0.75}Mo_{0.25}O_6$ and $Bi_2W_{0.25}Mo_{0.75}O_6$ nanostructures.

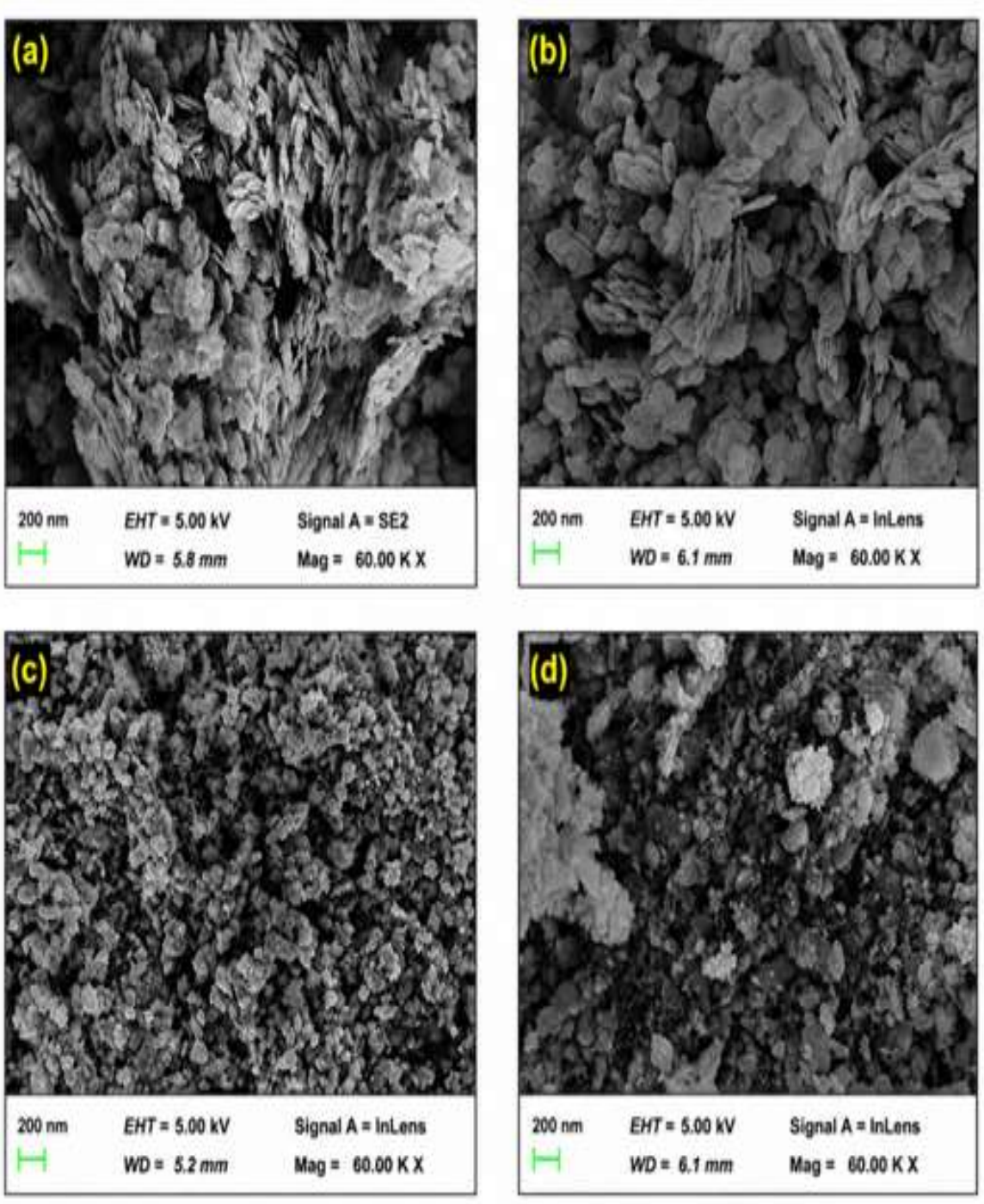

Figure 2. FESEM images (a) Bi_2WO_6, (b) Bi_2MoO_6, (c) $Bi_2W_{0.75}Mo_{0.25}O_6$ and(d) $Bi_2W_{0.25}Mo_{0.75}O_6$.

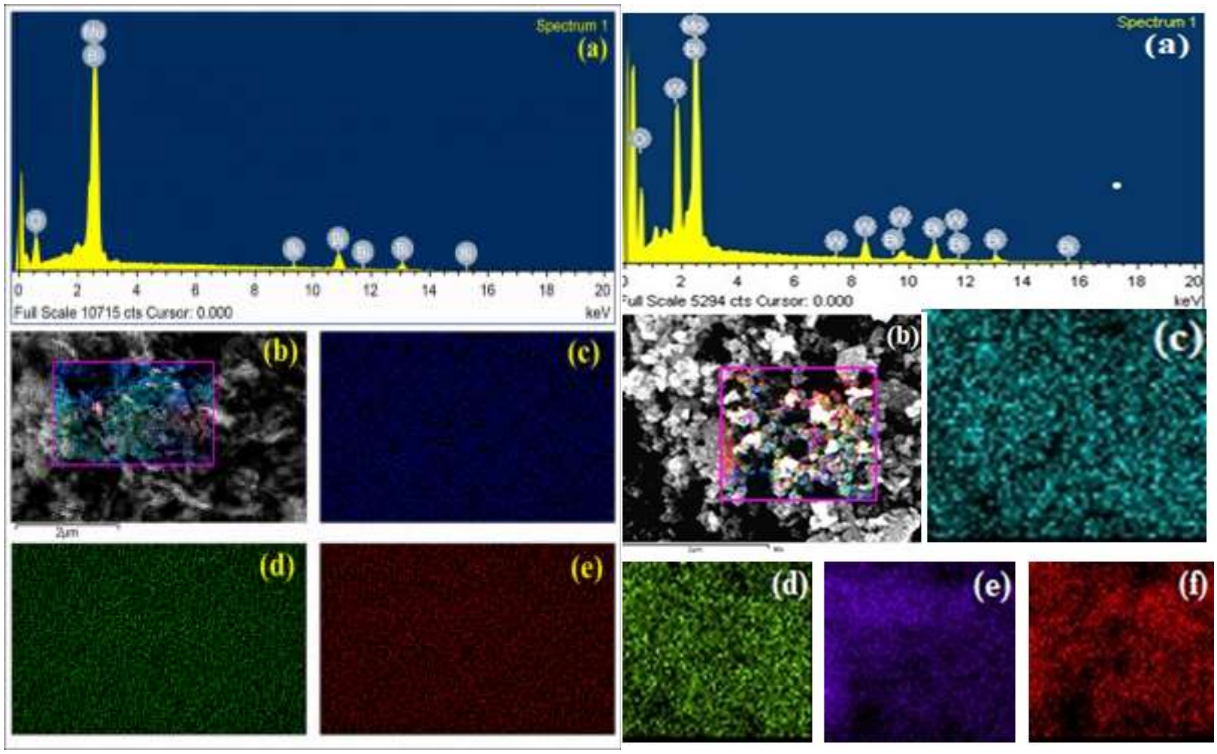

(i) **(ii)**

Figure 3. **(i)** (a) EDX spectra of $Bi_2W_{0.25}Mo_{0.75}O_6$, (b) Mixed colour mapping of $Bi_2W_{0.25}Mo_{0.75}O_6$ and colour mapping of elements (c) Bi, (d) Mo, (e) O. **(ii)** (a) EDX spectra of $Bi_2W_{0.75}Mo_{0.25}O_6$, (b) Mixed colour mapping of $Bi_2W_{0.75}Mo_{0.25}O_6$ and colour mapping of elements (c) Bi, (d) W, (e) O, (f) Mo

4.3. X-ray Photoelectron Spectra (XPS) Analysis

XPS was used to investigate the elemental composition and oxidation states of the constituent elements in the synthesized samples. For Bi_2MoO_6 and $Bi_2W_{0.25}Mo_{0.75}O_6$, the binding energy scale was calibrated using the C 1s signal located at 285 eV as the reference. The survey spectrum of Bi_2MoO_6 displayed characteristic signals corresponding exclusively to Bi, Mo, and O, confirming the presence of these elements in the sample, as presented in Figure 4(a).

The high-resolution Bi 4f spectrum of Bi_2MoO_6 (Figure 4(b)) exhibits two distinct peaks at 158.5 and 163.8 eV, corresponding to the Bi $4f_{7/2}$ and Bi $4f_{5/2}$ components, respectively. In the Mo 3d spectrum (Figure 4(c)), the characteristic peaks located at 232.2 and 235.5 eV are attributed to Mo $3d_{5/2}$ and Mo $3d_{3/2}$, respectively, confirming the presence of molybdenum in the +6 oxidation state. The O 1s spectrum shown in Figure 4(d) can be deconvoluted into three components centered at 530.9, 529.6, and 527.2 eV, which are associated with Bi–O bonding, hydroxyl groups (O–H), and oxygen-vacancy-related species, respectively [21]. The survey spectrum of $Bi_2W_{0.75}Mo_{0.25}O_6$ presented in Figure 5(a) reveals signals exclusively from Bi, W, Mo, and O, confirming the expected elemental composition. Furthermore, the high-resolution Bi 4f spectrum (Figure 5(b)) displays two prominent peaks at 160.0 and 165.2 eV, assigned to Bi $4f_{7/2}$ and Bi $4f_{5/2}$, respectively, thereby confirming that bismuth exists predominantly in the +3 oxidation state.

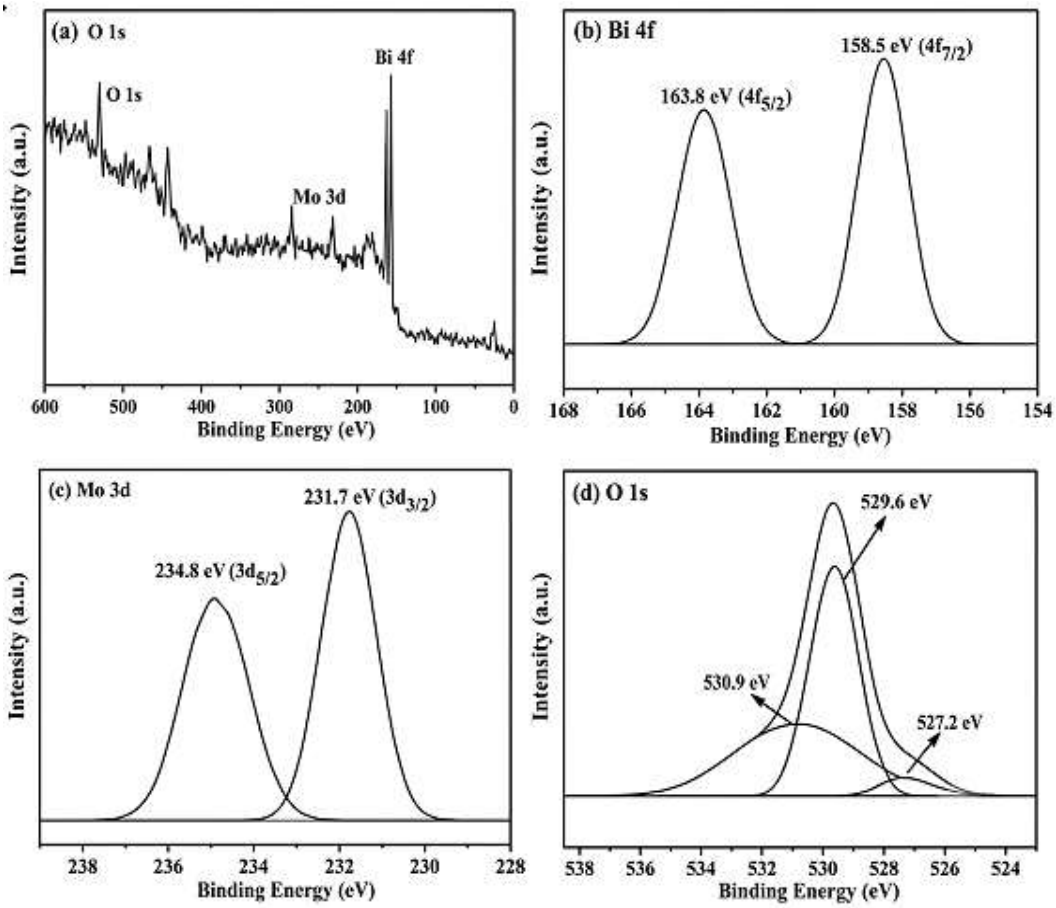

Figure 4. XPS spectra(a) survey spectrum, (b) Bi 4f, (c) W 4f, (d) O 1s, of Bi_2MoO_6

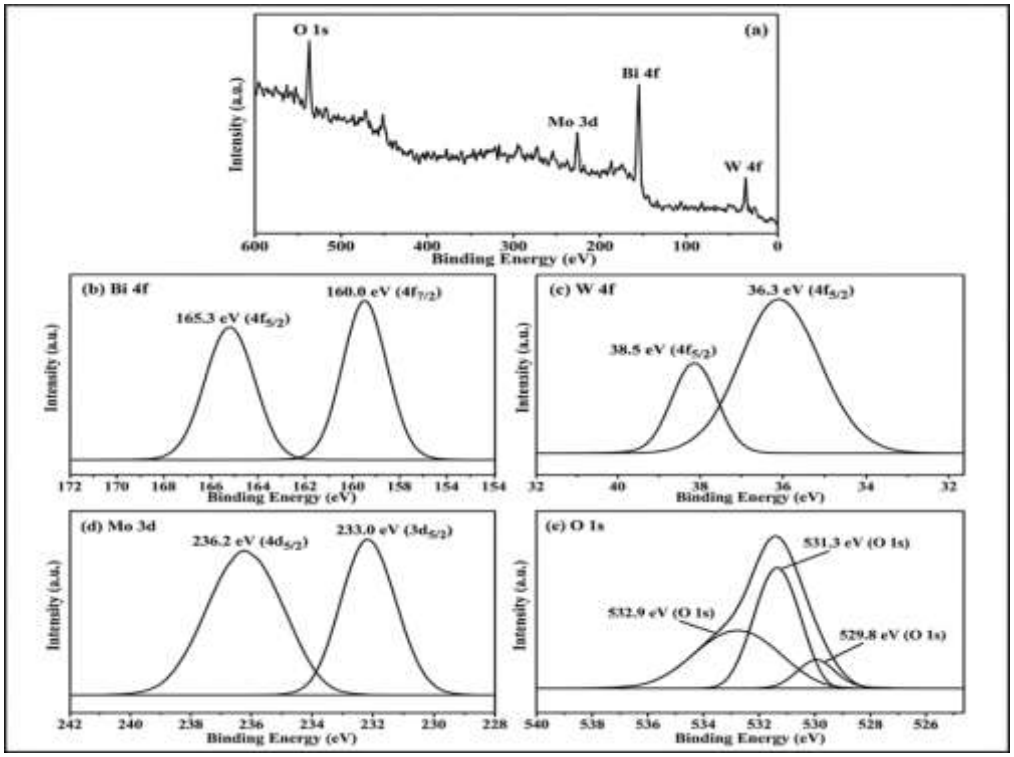

Figure 5. XPS spectra(a) survey spectrum, (b) Bi 4f, (c) W 4f, (d)Mo 3d (e) O 1s, of $Bi_2W_{0.25}Mo_{0.75}O$.

The high-resolution W 4f spectrum of $Bi_2W_{0.75}Mo_{0.25}O_6$ shown in Figure 5(c) displays two characteristic peaks at 36.3 and 38.5 eV, which are attributed to the W $4f_{7/2}$ and W $4f_{5/2}$ levels, respectively, confirming that tungsten exists predominantly in the +6 oxidation state. The corresponding Mo 3d spectrum in Figure 5(d) presents two distinct signals at 233.0 and 236.2 eV, assigned to the Mo $3d_{5/2}$ and Mo $3d_{3/2}$ components, respectively, indicating the presence of Mo^{6+} species. In addition, the O 1s spectrum shown in Figure 5(e) consists of three main contributions centered at 532.9, 531.3, and 529.8 eV. These peaks can be associated with surface oxygen environments related to lattice Bi–O bonds, O–Mo/W species, and chemisorbed hydroxyl (O–H) groups, respectively [22].

4.4. Fourier Transform Infrared Spectroscopy (FTIR)

FTIR spectra of the synthesized sample were measured over the wavenumber range of 1000–300 cm^{-1}, and the corresponding spectra are presented in Figure 6, with the observed peak positions summarized in Table 3.1. The Bi_2WO_6 sample exhibits characteristic absorption bands at 443, 583, 725, and 820 cm^{-1}. The bands appearing at 443 and 583 cm^{-1} can be attributed to Bi–O vibrational modes, whereas the signals at 725 and 820 cm^{-1} are associated with W–O stretching and W–O–W bending vibrations, respectively [12,23]. In the case of Bi_2MoO_6, four distinct bands are observed at 443, 583, 797, and 843 cm^{-1}, indicating the characteristic vibrational features of the Bi–Mo–O framework

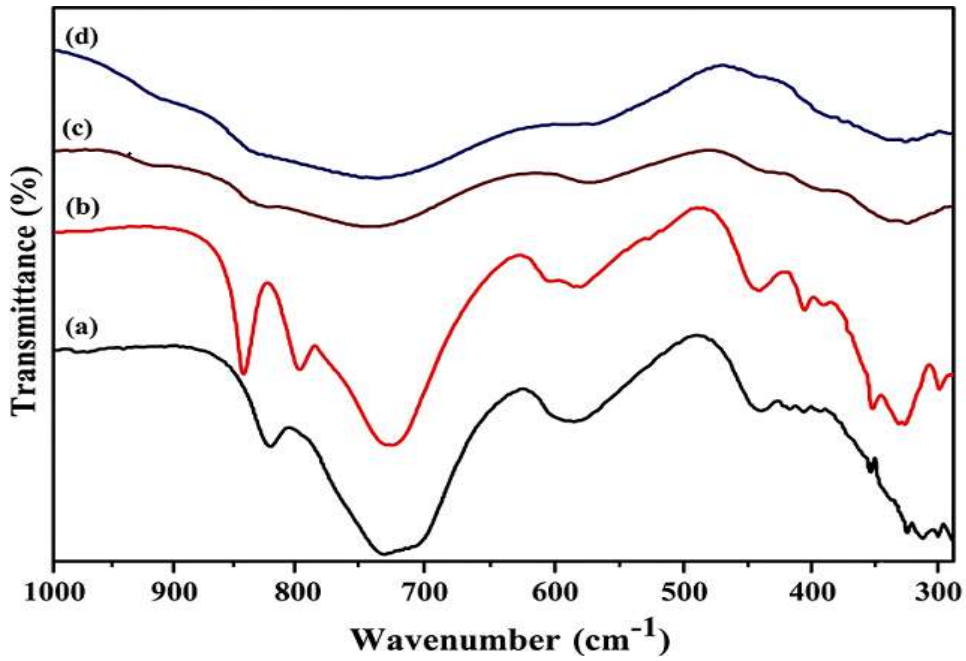

Figure 6. FTIR spectra of Bi_2WO_6, Bi_2MoO_6, $Bi_2W_{0.75}Mo_{0.25}O_6$ and $Bi_2W_{0.25}Mo_{0.75}O_6$.

Table 1: FTIR peak positions of all the compounds.

Sample Code	Wavenumber (cm^{-1})					
Bi_2WO_6	443	583	725	--	820	--
Bi_2MoO_6	443	583	725	797	--	843
$Bi_2W_{0.75}Mo_{0.25}O_6$	447	570	733	--	830	--
$Bi_2W_{0.25}Mo_{0.75}O_6$	450	568	730	--	832	--

The peak observed at 583 cm^{-1} can be assigned to the bending mode of Mo–O–Mo linkages present within the MoO_6 octahedral units. The bands located at 797 and 843 cm^{-1} correspond to the symmetric and asymmetric stretching vibrations of Mo–O bonds associated with apical oxygen atoms in the MoO_6 units, respectively. For the mixed oxides $Bi_2W_{0.75}Mo_{0.25}O_6$ and $Bi_2W_{0.25}Mo_{0.75}O_6$, characteristic bands appear at 447, 570, 733, and 830 cm^{-1}, and at 450, 568, 730, and 832 cm^{-1}, respectively. The displacement of these vibrational bands toward higher wavenumbers compared with those of Bi_2WO_6 suggests the substitution or incorporation of Mo^{6+} ions within the W^{6+}-based structural framework [24]. Notably, the characteristic Bi_2WO_6 band at 820 shifts to 830 cm^{-1} for $Bi_2W_{0.75}Mo_{0.25}O_6$ and to 832 cm^{-1} for $Bi_2W_{0.25}Mo_{0.75}O_6$. Such shifts can be attributed to changes in the metal–oxygen bond lengths and local bonding environments within the WO_6 and MoO_6 octahedral units containing apical oxygen atoms [22,25]. Overall, the observed variations in peak positions and vibrational features provide strong evidence for the successful formation of the intended mixed-metal oxide compounds.

4.5. UV-Vis Diffuse Reflectance Spectra

The optical characteristics of Bi_2WO_6, Bi_2MoO_6, $Bi_2W_{0.75}Mo_{0.25}O_6$, and $Bi_2W_{0.25}Mo_{0.75}O_6$ were investigated by UV–Vis DRS, and the corresponding spectra are presented in Figure 7. The absorption edge for each photocatalyst was estimated by drawing a tangent along the region exhibiting a sharp or gradual reduction in the absorption intensity and extrapolating it to intersect the wavelength axis. The absorption edge wavelengths obtained for Bi_2WO_6, Bi_2MoO_6, $Bi_2W_{0.75}Mo_{0.25}O_6$, and $Bi_2W_{0.25}Mo_{0.75}O_6$ were approximately 440, 454, 465, and 494 nm, respectively. These results indicate a progressive shift of the absorption edge toward longer wavelengths for the mixed compositions, suggesting enhanced utilization of the visible-light region.

These observations confirm that all the synthesized materials can effectively participate in visible-light-driven photocatalytic reactions through the excitation of electrons across their respective bandgap energies. The calculated optical bandgap values for Bi_2WO_6, Bi_2MoO_6, $Bi_2W_{0.75}Mo_{0.25}O_6$, and $Bi_2W_{0.25}Mo_{0.75}O_6$ are 2.81, 2.72, 2.66, and 2.51 eV, respectively. In addition, a distinct absorption feature centered at approximately 310 nm is observed in the UV–Vis spectra of Bi_2WO_6, Bi_2MoO_6, $Bi_2W_{0.75}Mo_{0.25}O_6$, and $Bi_2W_{0.25}Mo_{0.75}O_6$.

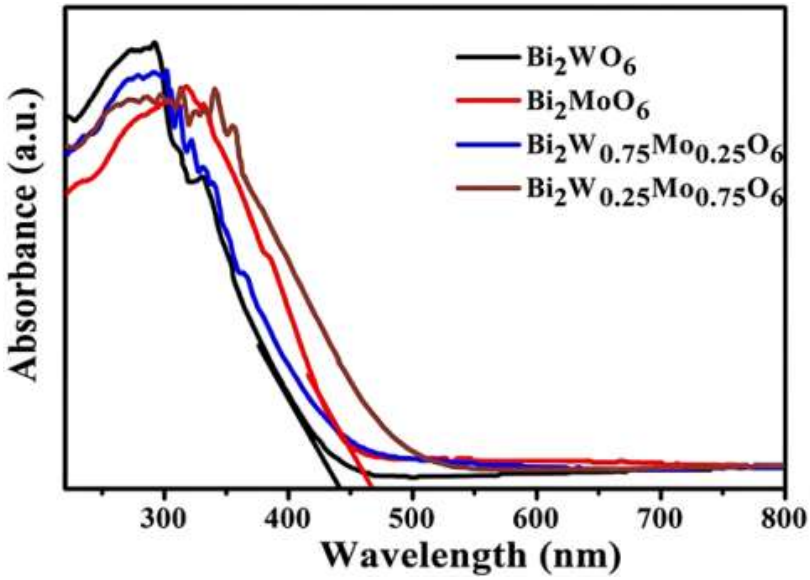

Figure 7. UV-Vis DRS spectra of Bi_2WO_6, Bi_2MoO_6, $Bi_2W_{0.75}Mo_{0.25}O_6$ and $Bi_2W_{0.25}Mo_{0.75}O_6$

The observed absorption is mainly attributed to ligand-to-metal charge transfer (LMCT) from O 2p orbitals to the W 5d, Mo 4d, or Bi 6p orbitals. The reduced bandgap facilitates electron excitation under visible light, leading to increased photogenerated charge carriers and improved photocatalytic activity. Consequently, the mixed oxides exhibit enhanced photocatalytic performance compared with the individual Bi_2WO_6 and Bi_2MoO_6 compounds.

5. Photocatalytic Activity and Estimates of Band Edge Potentials

Figure 8(a) presents the photocatalytic activity (PCA) of Bi_2WO_6, Bi_2MoO_6, $Bi_2W_{0.75}Mo_{0.25}O_6$, and $Bi_2W_{0.25}Mo_{0.75}O_6$, together with the blank experiment conducted in the absence of a catalyst, for the degradation of Methylene Blue (MB) under visible-light irradiation. The degradation was monitored at 30 min intervals for a total irradiation period of 240 min. As shown in Figure 8(b), only about 10% of MB degradation was observed in the blank experiment after 240 min, while the corresponding degradation efficiencies obtained with Bi_2WO_6, Bi_2MoO_6, $Bi_2W_{0.75}Mo_{0.25}O_6$, and $Bi_2W_{0.25}Mo_{0.75}O_6$ were 68%, 65%, 94%, and 96%, respectively. The mixed photocatalysts $Bi_2W_{0.75}Mo_{0.25}O_6$ and $Bi_2W_{0.25}Mo_{0.75}O_6$ exhibited considerably higher photocatalytic efficiencies than the individual Bi_2WO_6 and Bi_2MoO_6 phases, which may be related to differences in their band-edge potentials and charge-transfer characteristics. Moreover, the photocatalytic performances of Bi_2WO_6 and Bi_2MoO_6 are superior to those of several previously reported photocatalytic materials, as summarized in Table 2.

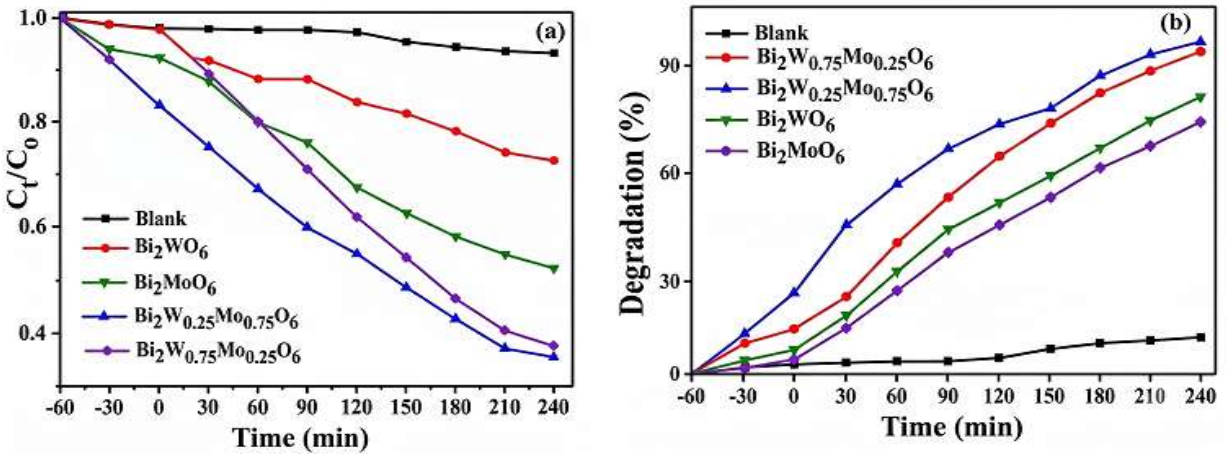

Figure 8. (a). Concentration changes of MB over Bi_2WO_6, Bi_2MoO_6, $Bi_2W_{0.75}Mo_{0.25}O_6$ and $Bi_2W_{0.25}Mo_{0.75}O_6$ photocatalysts along with the blank experiment. **(b).** Degradation % of MB in the presence of Bi_2WO_6, Bi_2MoO_6, $Bi_2W_{0.75}Mo_{0.25}O_6$ and $Bi_2W_{0.25}Mo_{0.75}O_6$ catalysts along with pure MB.

Table 2. Comparison of photocatalytic degradation with the other compounds in the literature

Compounds	Dye	Light source	Degradation	Time	Reference
TiO_2	MB	UV	50%	180mim	[26]
Zno-SnO_2	MB	Visible (100W)	49%	360min	[27]
Co_3O_4	MB	Visible	32%	180min	[28]
CeO_2/Bi_2WO_6	MB	Visible	54.9%	75min	[29]
Bi_2WO_6	MB	Visible (250W)	62%	22hrs	[30]
Bi_2MoO_6	MB	Visible (250W)	65%	240min	[31]
$Bi_2W_{0.75}Mo_{0.25}O_6$	MB	Visible (250W)	94%	240min	This work
$Bi_2W_{0.25}Mo_{0.75}O_6$	MB	Visible (250W)	96%	240min	This work

The photocatalytic degradation of MB followed a pseudo-first-order kinetic model, with $\ln(C_0/C_t)$ plotted against irradiation time (t), as shown in Figure 9. The corresponding rate constants were 0.000230, 0.000891, 0.000596, 0.00361, and 0.00375 min^{-1} for the blank, Bi_2WO_6, Bi_2MoO_6, $Bi_2W_{0.75}Mo_{0.25}O_6$, and $Bi_2W_{0.25}Mo_{0.75}O_6$, respectively. The higher rate constants of the mixed oxides confirm their enhanced photocatalytic efficiency.

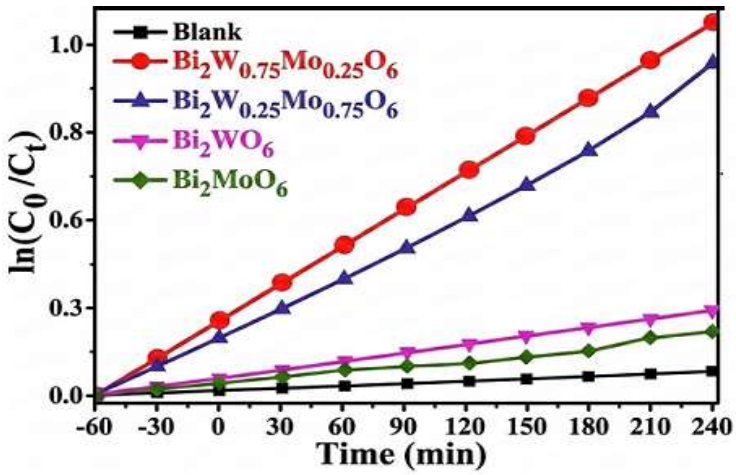

Figure 9. The first order kinetics plots of the degradation of MB for all synthesized compounds

According to the kinetic results, $Bi_2W_{0.75}Mo_{0.25}O_6$ and $Bi_2W_{0.25}Mo_{0.75}O_6$ exhibited the highest MB degradation rate constants of approximately 0.003361 and 0.00376 min^{-1}, respectively. These two photocatalysts were selected to investigate the variation in the MB absorption profile with irradiation time, as shown in Figure 10(a–b). The gradual reduction in absorption intensity with increasing irradiation time confirms the progressive degradation of MB under visible-light irradiation [32].

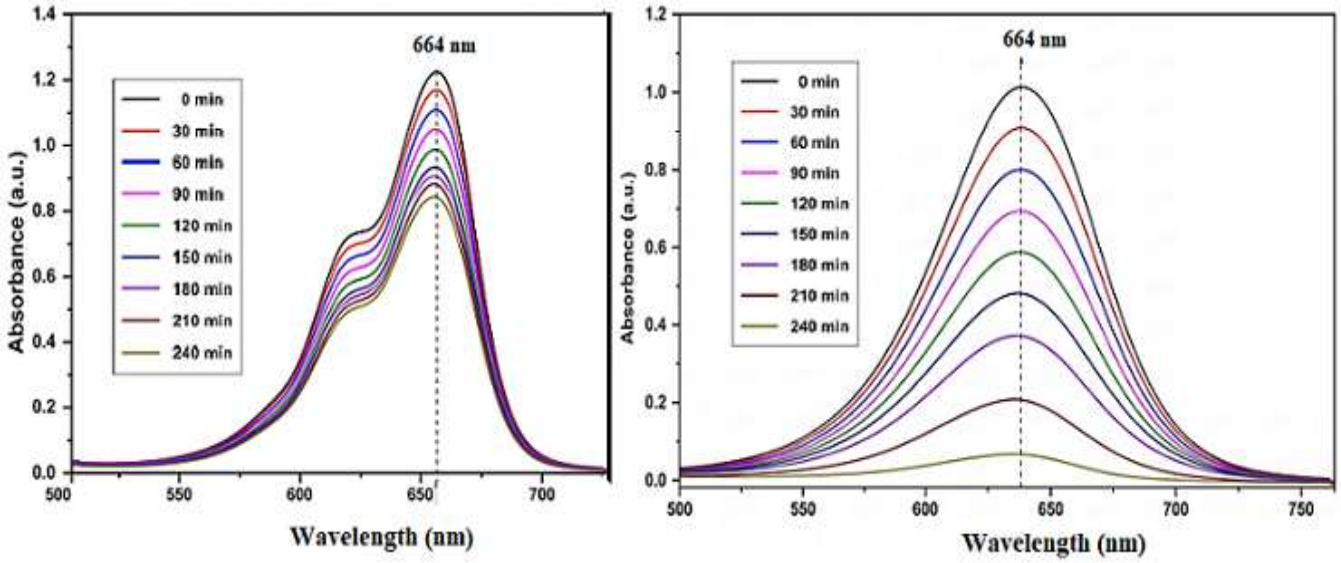

Figure 10. Time–dependent UV-Vis absorption spectra of Rh B (a) without catalyst (b) Bi_2MoO_6

The photocatalytic efficiency of semiconductor materials is closely associated with the generation, migration, and recombination of photogenerated electron–hole pairs. A high electron–hole recombination rate generally results in a lower concentration of charge carriers available for surface

redox reactions, thereby reducing photocatalytic performance, whereas suppressed recombination promotes efficient charge separation and enhances photocatalytic activity [33]. To investigate the charge-carrier recombination behavior of the synthesized photocatalysts, photoluminescence (PL) measurements were performed using an excitation wavelength of 330 nm. The PL spectra of Bi_2WO_6, Bi_2MoO_6, $Bi_2W_{0.75}Mo_{0.25}O_6$, and $Bi_2W_{0.25}Mo_{0.75}O_6$ are presented in Figure 11. All four photocatalysts exhibit a prominent emission band centered at approximately 430 nm, which can be associated with the radiative recombination of photogenerated charge carriers. The intensity of the PL emission provides useful information about the recombination probability of electrons and holes. Compared with the parent Bi_2WO_6 and Bi_2MoO_6 materials, the mixed oxides $Bi_2W_{0.75}Mo_{0.25}O_6$ and $Bi_2W_{0.25}Mo_{0.75}O_6$ display substantially weaker PL emission.

The reduced PL intensity indicates that the incorporation of Mo and W into the mixed oxide structure facilitates more effective separation of photogenerated electrons and holes and suppresses their direct recombination. Consequently, a greater number of charge carriers can reach the catalyst surface and participate in the formation of reactive oxygen species, such as $\bullet O_2^-$ and h^+, which are responsible for the degradation of MB. Therefore, the PL results are consistent with the photocatalytic degradation experiments, in which the mixed oxides exhibited significantly higher MB removal efficiencies than the individual Bi_2WO_6 and Bi_2MoO_6 photocatalysts. These findings demonstrate that improved charge-carrier separation is one of the important factors contributing to the enhanced visible-light photocatalytic performance of the mixed Bi-based oxides [34].

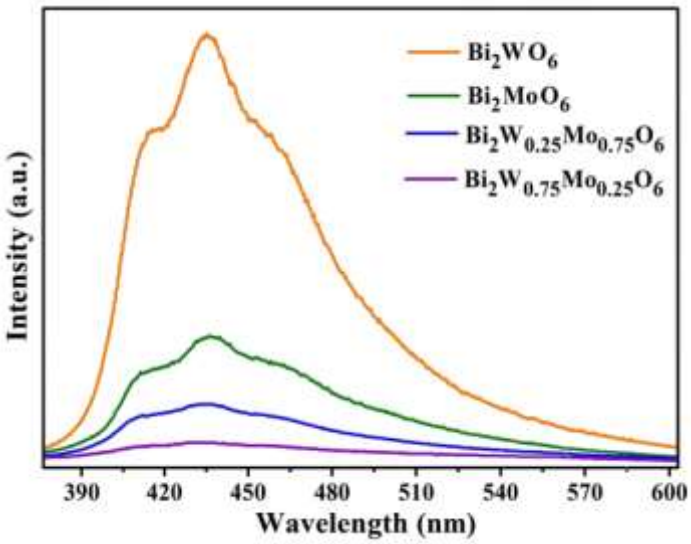

Figure 11. Photoluminescence (PL) spectra of (a) Bi_2WO_6, (b) Bi_2MoO_6, (c) $Bi_{0.75}Mo_{0.25}O_6$ and (d) $Bi_2W_{0.25}Mo_{0.75}O_6$

6. Reactive Species Scavenging Test

To identify the active reactive species responsible for the photocatalytic degradation of MB, scavenger experiments were conducted using specific trapping agents. Benzoquinone (BQ), ammonium oxalate (AO), and tert-butanol (TBT) were employed as scavengers for superoxide radicals ($\bullet O_2^-$), photogenerated holes (h^+), and hydroxyl radicals ($\bullet OH$), respectively [30]. Since $Bi_2W_{0.75}Mo_{0.25}O_6$ and $Bi_2W_{0.25}Mo_{0.75}O_6$ exhibited the highest photocatalytic efficiencies, these two catalysts were separately treated with the selected scavengers at the prescribed concentrations. The photocatalytic degradation

experiments were then repeated under visible-light irradiation, and the resulting degradation efficiencies are presented as bar charts in Figure 12(a) and (b). The changes in MB degradation after the addition of individual scavengers provide valuable information about the major reactive species involved in the photocatalytic reaction mechanism.

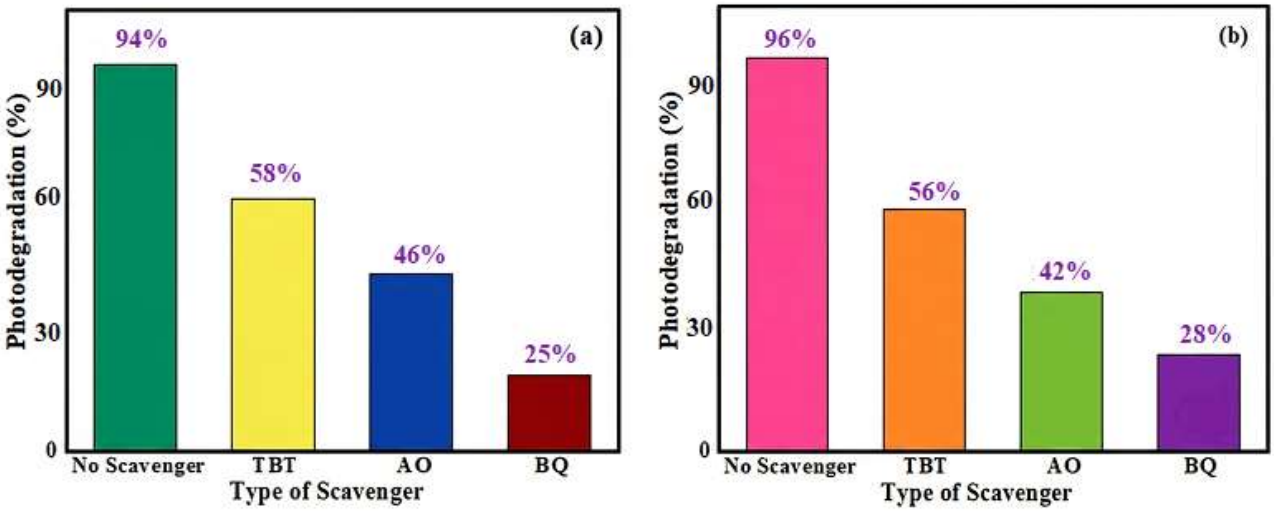

Figure 12. Photocatalytic degradation (%) of MB using different scavengers over (a) $Bi_2W_{0.75}Mo_{0.25}O_6$ and (b) $Bi_2W_{0.25}Mo_{0.75}O_6$

The inhibition of MB degradation caused by the different scavengers followed the order BQ > AO > TBT, indicating that benzoquinone produced the greatest reduction in photocatalytic activity. The stronger suppression observed in the presence of BQ suggests that superoxide radicals ($\bullet O_2^-$) make a major contribution to the degradation of MB. Ammonium oxalate also caused a considerable decrease in dye removal, demonstrating the important involvement of photogenerated holes (h^+) in the degradation pathway. In contrast, the relatively smaller effect of tert-butanol indicates a comparatively minor contribution from hydroxyl radicals (•OH). Therefore, the scavenger experiments confirm that $\bullet O_2^-$ and h^+ are the predominant reactive species responsible for the visible-light-driven degradation of MB [35].

7. Conclusions

Bi_2WO_6, Bi_2MoO_6, $Bi_2W_{0.75}Mo_{0.25}O_6$, and $Bi_2W_{0.25}Mo_{0.75}O_6$ were successfully synthesized through a one-pot hydrothermal route. Among the prepared materials, $Bi_2W_{0.75}Mo_{0.25}O_6$ and $Bi_2W_{0.25}Mo_{0.75}O_6$ exhibited superior photocatalytic performance toward the degradation of MB under visible-light irradiation. XRD characterization confirmed the successful formation and crystalline nature of the synthesized compounds, while FTIR analysis provided evidence for their characteristic chemical bonding and vibrational modes. UV–Vis diffuse reflectance measurements demonstrated broad visible-light absorption, which contributes to the enhanced photocatalytic activity of these materials. Furthermore, scavenger experiments performed with the highly active mixed oxides confirmed the significant involvement of photogenerated holes (h^+) and superoxide radicals ($\bullet O_2^-$) in the MB degradation process. Overall, the mixed Bi-based oxides demonstrated promising potential as efficient visible-light-responsive photocatalysts for dye removal.

References

1. He H.Y., Lu J., Zhao L., Preparation and photocatalytic activity of Bi_2WO_6 particles synthesized by
2. hydrothermal method, Desalination, 252(1–3), 66–70, 2010.
3. Xu Y., Langford C.H., Enhanced photoactivity of titanium dioxide supported on bacterial cellulose
4. film, Langmuir, 17(3), 897–902, 2001.
5. Zhang X., Liu Y., Wang Z., Synthesis and photocatalytic properties of novel bismuth-based semiconductor heterojunctions, Molecules, 20, 4911, 2024.
6. Fujishima A., Honda K., Electrochemical photolysis of water at a semiconductor electrode, Nature, 238(5358), 37–38, 1972.
7. Mao W., Chen X., Zhang Y., Advanced oxidation processes for organic pollutant degradation: Mechanism and environmental application, Frontiers of Environmental Science & Engineering, 18(7), 86, 2024.
8. Liuying L., Zhao M., Sun H., Sonocatalytic degradation of organic dyes over nanostructured catalysts: A comparative study, Ultrasonics Sonochemistry, 39, 93–100, 2017.
9. Chen F., Ma T., Zhang L., Atomic-level design of photocatalytic materials for energy conversion and environmental remediation, Advanced Materials, 33(12), 2005256, 2021.
10. Hoang L.H., Cho S., Park J., Hydrothermal synthesis and characterization of bismuth tungstate nanostructures for visible-light photocatalysis, Journal of Materials Science: Materials in Electronics, 28, 12191–12196, 2017.
11. Wang S., Gu Y., Liu X., Engineering interfacial charge transfer in nanostructured heterojunctions for highly efficient photocatalysis, Small Structures, 2(4), 2000061, 2021.
12. Sun Y., Zhou Q., Li R., Recent progress in visible-light-driven bismuth-based photocatalysts for water purification, Molecules, 7, 3123, 2023.
13. Dong S.Y., Zhang J., Huang T., Construction of Z-scheme heterojunction photocatalysts and their boosted degradation efficiency for organic pollutants, Chemical Engineering Journal, 316, 778–789, 2017.
14. Zhang P., Wang H., Liu C., Solthermal synthesis of hierarchical bismuth molybdate nanostructures and their photocatalytic performance, Ceramics International, 42(15), 16749–16757, 2016.
15. Issarapanacheewin S., Wetchakun K., Wetchakun N., Synthesis, characterization, and photocatalytic activity of Bi_2WO_6/Bi_2MoO_6 heterojunctions, Ceramics International, 42(14), 16007–16016, 2016.
16. Bi_2WO_6 nanosheets, Applied Surface Science, 391, 194–201, 2017.
17. Liu X.N., Su Y., Chen Y., Enhanced photocatalytic activity of Bi_2WO_6 nanostructures modified with noble metal nanoparticles, Journal of Alloys and Compounds, 662, 598–606, 2016.
18. Zhang F.J., Zhang C., Zhou Y., Photocatalytic degradation of organic pollutants under visible light using bismuth-based catalysts, Separation and Purification Technology, 113, 1–8, 2013.
19. Song X.C., Zheng X.F., Zhang Y., Synthesis and photocatalytic activity of novel bismuth-containing composite materials, Materials Science and Engineering: B, 197, 31–35, 2015.
20. Cullity B.D., Elements of X-ray Diffraction, 2nd ed., Addison-Wesley, 96–99, 1978.
21. Xuetao Y., Zhang L., Zhao W., Interfacial charge regulation in 2D/2D heterojunctions for efficient solar-driven pollutant degradation, ACS Applied Materials & Interfaces, 13, 19864–19872, 2021.
22. Selvarajan S., Suganthi A., Rajarajan M., Fabrication of visible-light active heterojunction photocatalysts for the removal of toxic organic dyes, Journal of Industrial and Engineering Chemistry, 53, 201–212, 2017.

23. Zhang L., Wang H., Chen Z., Bi_2WO_6 nano-crystals: Hydrothermal preparation, characterization and photocatalytic properties, Applied Catalysis B: Environmental, 98(3–4), 138–146, 2010.
24. Pascariu P., Cojocaru C., Olaru N., Novel electrospun composite nanofibers for efficient photocatalytic degradation of organic contaminants, Ceramics International, 42(6), 6775–6781, 2016.
25. Dumrongrojthanath P., Thanachayanont C., Inceesungvorn B., Microwave-assisted synthesis of Bi_2WO_6 nanoparticles and their enhanced photocatalytic activity, Journal of the Ceramic Society of Japan, 126, 87–90, 2018.
26. Huang Y., Liang Y., Zhou M., Construction of novel bismuth-based heterostructures for photocatalytic application, ChemistrySelect, 3(26), 7423–7428, 2018.
27. Dileep M., Prasad K., Rao V., Structural, optical and visible-light photocatalytic properties of synthesized bismuth tungstate nanostructures, Ceramics International, 45(17), 22253–22263, 2019.
28. Entezari M., Naimi-Jamal M.R., Ghows N., Sonochemical synthesis of nanostructured photocatalysts for water treatment applications, Journal of Water Process Engineering, 32, 100983, 2019.
29. Li X., Jiang Y., Sun X., Controlled synthesis and enhanced visible-light photocatalytic performance of Bi_2WO_6 micro/nanostructures, Journal of Alloys and Compounds, 709, 285–292, 2017.
30. Etogo A., Huang H., Zhang Y., Hydrothermal synthesis of porous bismuth-based catalysts with boosted photocatalytic efficiency, Journal of Materials Chemistry A, 4(34), 13242–13250, 2016.
31. Chang X., Wang L., Liu Y., Recent advances in heterojunction engineering for photo-assisted environmental remediation, Applied Catalysis B: Environment and Energy, 349, 123858, 2024.
32. Shivani, V., et al. "Highly efficient 3-D hierarchical Bi2WO6 catalyst for environmental remediation." *Applied Surface Science* 488, 696-706, 2019.
33. Hao, Liang, and Jingfei Luan. "The fabrication and property characterization of a Ho2YSbO7/Bi2MoO6 heterojunction photocatalyst and the application of the photodegradation of diuron under visible light irradiation." *International Journal of Molecular Sciences* 25.8 4418,2024.
34. Dhas C.R., Venkatesh R., Raj A.M.E., Synthesis and characterization of nanostructured metal oxides for dye degradation, Ceramics International, 41(8), 9301–9313, 2015.
35. Phuruangrat A., Thongtem S., Thongtem T., Synthesis and photocatalytic activity of Bi_2WO_6 nanostructures by microwave-hydrothermal method, Journal of Materials Science: Materials in Electronics, 34, 16849, 2023.
36. Kaur A., Sharma S., Singh J., Advanced functional materials for photocatalytic detoxification of industrial wastewater, Chemosphere, 349, 140862, 2024.
37. Issarapanacheewin S., Wetchakun K., Wetchakun N., Enhanced photocatalytic degradation of organic pollutants over Bi_2WO_6/Bi_2MoO_6 heterojunctions, Ceramics International, 42(14), 1600716016, 2016